Probing $Ca_3Ti_2O_7$ crystal structure at the atomic level: Insights from perturbed angular correlation spectroscopy and *ab initio* studies

P. Rocha-Rodrigues [1,*] I. P. Miranda [2,†] S. S. M. Santos [3] G. N. P. Oliveira [1] T. Leal,[1] M. L. Marcondes [4]
J. G. Correia [5] L. V. C. Assali [4] H. M. Petrilli [4] A. M. L. Lopes [1,‡] and J. P. Araújo [1]

[1]*IFIMUP, Institute of Physics for Advanced Materials, Nanotechnology and Photonics, Departamento de Física e Astronomia da Faculdade de Ciências da Universidade do Porto, Rua do Campo Alegre, 687, 4169-007 Porto, Portugal*

[2]*Department of Physics and Astronomy, Uppsala University, Box 516, SE-75120 Uppsala, Sweden*

[3]*Escola Politécnica, Universidade de São Paulo, CEP 05508-010, São Paulo, SP, Brazil*

[4]*Instituto de Física, Universidade de São Paulo, CP 66318, 05315-970, São Paulo, SP, Brazil*

[5]*C²TN, Centro de Ciências e Tecnologias Nucleares, Departamento de Engenharia e Ciências Nucleares, Instituto Superior Técnico, Universidade de Lisboa, Estrada Nacional 10, 2695-066 Bobadela LRS, Portugal*

Perturbed angular correlation spectroscopy combined with *ab initio* electronic structure calculations is used to unravel the structural phase transition path from the low-temperature polar structure to the high-temperature structural phase in $Ca_3Ti_2O_7$, a hybrid improper ferroelectric. The experimental procedure, conducted at ISOLDE, explores the unique features of a local probe environment approach by monitoring the evolution of the electric field gradient tensor at the calcium sites. The local environments, observed above 1057 K, confirm a structural phase transition from the $A2_1am$ symmetry to an orthorhombic $Acaa$ symmetry in the $Ca_3Ti_2O_7$ crystal lattice, disagreeing with the frequently reported avalanche structural transition from the polar $A2_1am$ phase to the aristotype $I4/mmm$ phase. Moreover, the EFG temperature dependency, within the $A2_1am$ temperature stability, is shown to be sensitive to the recently proposed $Ca_3Ti_2O_7$ ferroelectric polarization decrease within the 500–800 K temperature range.

DOI: 10.1103/PhysRevB.109.224101

I. INTRODUCTION

The Ruddlesden-Popper (RP) $Ca_3Ti_2O_7$ compound was predicted by Benedek and Fennie, in 2011, to be a prototypical hybrid improper ferroelectric system through first-principles density functional theory (DFT) calculations [1]. The experimental confirmation of hybrid improper ferroelectricity (HIF) came later, in 2015, from the research group of Oh *et al.* [2]. They measured a ferroelectric polarization of approximately $8\,\mu C/cm^2$ while probing distinct orthorhombic twin domains observed in $Ca_3Ti_2O_7$ single crystals.

The discovery of HIF in this naturally layered perovskite (NLP) has prompted the scientific community to revisit other NLP systems and investigate the nature of structural transitions that they undergo in response to external stimuli, such as temperature or pressure [3–9].

The structural phase transition sequence that $Ca_3Ti_2O_7$ follows to reach the polar symmetry, as the temperature decreases, remains controversial. The $Ca_3Ti_2O_7$ crystal has been assumed to undergo an avalanche structural transition from the high-symmetry $I4/mmm$ phase to the low-symmetry polar $A2_1am$ phase through two distinct rotation and tilting modes of the TiO_6 octahedra that condense simultaneously upon cooling from high temperatures [11,12]. These

distortion modes are depicted in Fig. 1. Using differential scanning calorimetry (DSC), Liu *et al.* [11] revealed a first-order structural transition associated with the detection of an endothermic peak at 1099.5 K and an exothermic peak at 1082.5 K, measured for warming and cooling steps, respectively. Moreover, Gao *et al.* [12] estimated, from electrical resistivity measurements performed on a $Ca_3Ti_2O_7$ single crystal, that the transition between the undistorted $I4/mmm$ and the distorted $A2_1am$ structures should occur around 1063 K upon warming, and 1039 K, when cooling the samples. Kratochvilova *et al.* [6] conducted synchrotron x-ray powder diffraction (XRD) measurements on the $Ca_{3-x}Sr_xTi_2O_7$ series and reported that for $x < 0.6$ a direct structural transition from the ferroelectric $A2_1am$ phase to the paraelectric undistorted $I4/mmm$ is observed. Senn *et al.* [5] initially ascribe the phase transition to a decomposition of the sample but, in subsequent follow-up work, Pomiro *et al.* [7] proposed a strongly first-order phase transition to $Acca$ instead. They claimed that the $Ca_3Ti_2O_7$ undergoes a first-order structural transition from the $A2_1am$ to the $Acaa$ orthorhombic phase, rather than to the aristotype $I4/mmm$ structure, suggesting that the $Ca_3Ti_2O_7$ system should follow the same structural transition path as the $Ca_3Mn_2O_7$ isostructural compound [5,14]. The coexistence of the $A2_1am$ and $Acaa$ structural phases within the 1062.5 K to 1225 K temperature range was proposed [7]. More recently, using high-resolution neutron time-of-flight (nTOF) scattering combined with DSC experiments, Kong *et al.* [13] reported that $Ca_3Ti_2O_7$ displays the $Acaa$ symmetry for temperatures above 1082 K. However, unlike Pomiro *et al.*

---

*pedro.rodrigues@fc.up.pt
†ivan.miranda@alumni.usp.br
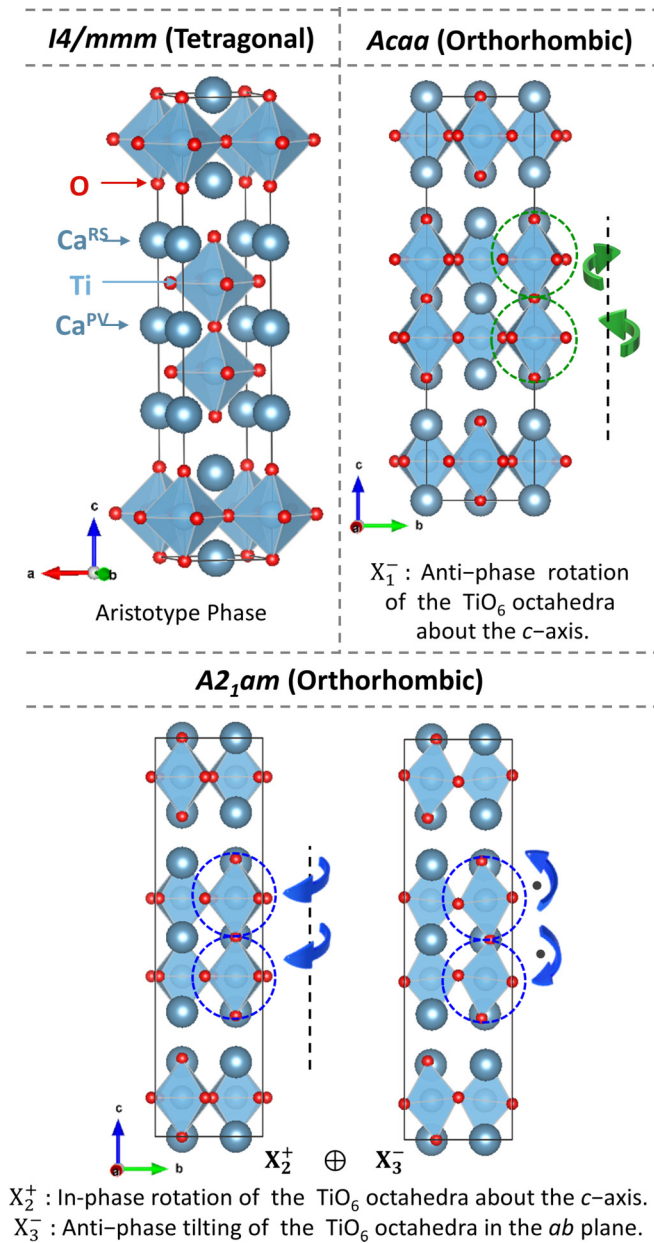‡armandina.lopes@fc.up.pt

X$_1^-$: Anti–phase rotation of the TiO$_6$ octahedra about the *c*–axis.

X$_2^+$ ⊕ X$_3^-$

X$_2^+$: In-phase rotation of the TiO$_6$ octahedra about the *c*–axis.
X$_3^-$: Anti–phase tilting of the TiO$_6$ octahedra in the *ab* plane.

FIG. 1. Representation of the Ca$_3$Ti$_2$O$_7$ crystal structure for the aristotype tetragonal *I4/mmm* symmetry and of the octahedral rotation and tilting modes for the orthorhombic *Acaa* and *A2$_1$am* space groups. The crystal structure was drawn using VESTA [10].
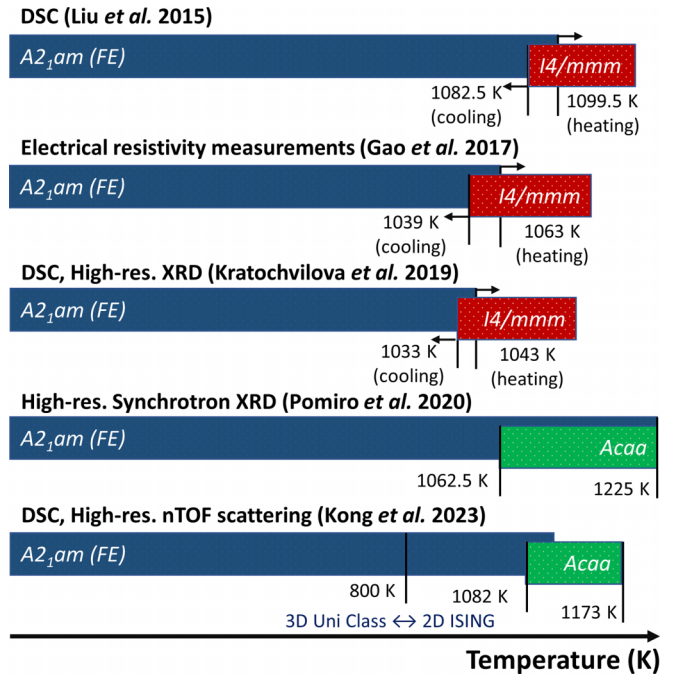

FIG. 2. Summary of the Ca$_3$Ti$_2$O$_7$ high-temperature structural transitions, as reported in a few of the selected studies [6,7,11–13].

The combined use of nanoscopic scale nuclear spectroscopy techniques, such as γ-γ perturbed angular correlation (PAC), and *ab initio* calculations has proven effective for probing local atomic phenomena. This approach elucidates the atomic environment by monitoring the electric field gradient (EFG) tensor at specific nuclear sites, as demonstrated in recent studies [14–18]. Specifically, in homologous Ruddlesden-Popper (RP) structures, the analysis of EFG distributions at the Ca sites across distinct temperatures, using radioactive ^{111m}Cd isotopes as probes, has provided insights into the octahedral rotation modes that underlie the materials' structural phase transitions and their functional properties [14,16].

In the present study, we explore the structural phase transition pathways of the Ca$_3$Ti$_2$O$_7$ compound. PAC investigations were conducted over a broad temperature range, from $10 - 1200$ K, employing ^{111m}Cd nuclei as probes. The experimental observations were combined with simulations within the DFT framework and the supercell scheme for Cd-ion substitution.

II. METHODOLOGY

A. Experimental details

Polycrystalline samples of Ca$_3$Ti$_2$O$_7$ were synthesized using the solid-state reaction method. Stoichiometric amounts of CaCO$_3$ (99.0%, Sigma-Aldrich) and TiO$_2$ (99.99%, Sigma-Aldrich) were mixed and subjected to calcination at 1123 K for 3 hours in air. This was followed by a series of grinding, pelletizing, and annealing at 1773 K for 6 hours, repeated several times to ensure homogeneity and phase purity. The phase composition was verified through Le Bail refinement of x-ray powder diffraction data, collected using a Rigaku

that reported a broad temperature *A2$_1$am* and *Acaa* coexistence, at 1173 K solely the *Acaa* structural phase was reported to persist. The analysis of temperature-dependent evolution of Ca$_3$Ti$_2$O$_7$ ferroelectric polarization, as estimated from the Rietveld refinements, allowed the identification of a second critical temperature at 800 K. Below 800 K, Kong *et al.* proposed that the polarization behavior of Ca$_3$Ti$_2$O$_7$ transitions from a two-dimensional Ising system to a three-dimensional universality class, where the polarization suffers a significant increase while cooling in the 500–800 K range [13]. A summary of the high-temperature structural transitions proposed for Ca$_3$Ti$_2$O$_7$, along with the respective critical temperatures, is displayed in Fig. 2.

SmartLab diffractometer and analyzed with the Fullprof software package [19], as detailed in Appendix A.

Given the short lifetime of 48.5 min of the ^{111m}Cd parent probe, performing a PAC measurement at each temperature required an implantation-annealing-measurement cycle at the ISOLDE-CERN facility [20]. Experiments were conducted on approximately 4 mm^3 samples, all obtained from the synthesized pellet. Ion beam implantation of ^{111m}Cd isotopes with an energy of 30 keV, up to a low dose of 10^{11} ions/cm^2. The ^{111m}Cd probe should substitute Ca^{2+} in perovskite systems since it has a similar ionic radius and charge, facilitating accurate PAC measurements [14,16,21]. After each implantation step, a 20-minute thermal annealing was performed in air, typically within the $1100 - 1123$ K temperature range, to eliminate implantation-induced defects. Each PAC measurement was carried out for a ~ 3 h acquisition time, using a six-detector angular correlation setup [22]. For experiments conducted below room temperature, the samples were kept under vacuum using a He closed-cycle refrigerator to reach the desired measurement temperatures through cooling. For experiments above room temperature, a high-temperature furnace exposed the samples to an air atmosphere, achieving the aimed measurement temperatures through heating.

The ^{111m}Cd probes decay to stable ^{111}Cd through an intermediate state by emitting two consecutive γ photons. The half-life of the parent state is 48.5 min, while the intermediate state has a half-life of 84.5 ns [23]. In the absence of hyperfine interaction, the probability of detecting the second γ ray (γ_2) at an angle θ relative to the direction of the first emitted γ ray (γ_1), exhibits a characteristic anisotropic angular distribution. This distribution can be described by an expansion in Legendre polynomials [$P_k(\cos\theta)$] and the angular correlation coefficients characteristic of the nuclear decay cascade [$A_{kk}(\gamma_1, \gamma_2)$] [23]. In the presence of hyperfine interactions, between the electric quadrupole moment of the nucleus in the intermediate state and the EFG at the nuclear site, the γ-γ anisotropic angular distribution [$W(\theta, t)$] becomes time dependent and for polycrystalline systems can be described as [24]

$$W(\theta, t) = e^{-t/\tau_N} \sum_k A_{kk}(\gamma_1, \gamma_2) P_k(\cos\theta) G_{kk}(t). \quad (1)$$

Here, τ_N is the intermediate state half-life, and $G_{kk}(t)$ is the time-perturbation factor containing the information about the hyperfine interactions affecting the intermediate state of the nuclear decay. By using a six-detector angular correlation apparatus, the time-dependent perturbation can be measured and used to estimate the strength and symmetry of the EFG [22].

The EFG is the second derivative of the Coulomb potential at a given nuclear site and gives information on the local charge distribution, being a second-order traceless symmetric tensor V_{ij}, that can be diagonalized (principal reference frame), with the convention $|V_{zz}| \geqslant |V_{yy}| \geqslant |V_{xx}|$. Accordingly, it is usually described by two parameters, the principal component V_{zz} and the asymmetry parameter $\eta = (V_{xx} - V_{yy})/V_{zz}$ [25]. In polycrystalline systems and static electric quadrupole interactions, the time-perturbation factor can be described as a sum of periodic terms according to the expression

$$G_{kk}(t) = s_{k0} + \sum_{n=1}^{3} s_{kn} \cos(\omega_n t) e^{-\delta\omega_n t}, \quad (2)$$

where t is the time spent by the nucleus in the ^{111m}Cd intermediate probing state, i.e., the time interval between the pair of γ_1 and γ_2 photons detection, and the ω_n are related to the transition frequencies between the hyperfine levels when the intermediate nuclear state is split by the hyperfine interaction. The ^{111m}Cd probing level is characterized by an $I = 5/2$ nuclear spin momentum, which is split by the electric quadrupole interaction into three sublevels. Consequently, in the Fourier transforms (FTs) of the $G_{kk}(t)$ functions, a triplet of frequencies, ω_1, ω_2, and $\omega_3 = \omega_1 + \omega_2$, is observed for each nonvanishing EFG present in the system. The damping term in Eq. (2) can be related to the presence of randomly distributed vacancies, defects, and lattice strains; therefore, the ω_n transition frequencies are characterized by a δ relative width about a mean value and each local environment can be described by an EFG Lorentzian-like distribution.

The ω_n transition frequencies and the s_{kn} correspondent amplitudes are related with the fundamental quadrupolar frequency ω_0 [24]. Explicitly, one can define $\omega_n = g_n(\eta)\omega_0$, where $g_n(\eta)$ and $s_{kn} = s_{kn}(\eta)$ [Eq. (2)] are known functions of the asymmetry parameter [26]. In the particular case of $\eta = 0$, the fundamental quadrupolar frequency matches the lower observable, i.e., $\omega_1 = \omega_0$, being $\omega_2 = 2\omega_0$ and $\omega_3 = 3\omega_0$. The fundamental quadrupolar frequency, from which we obtain the strength of the EFG, main component $|V_{zz}|$, is defined as

$$\omega_0 = \frac{3eQV_{zz}}{2I(2I-1)\hbar}, \quad (3)$$

where Q is the nuclear electric quadrupole moment of the ^{111m}Cd probe in the intermediate level. For the calculation of $|V_{zz}|$, we have used the well-known $Q = 0.83(13)$ b value [25], in compliance with earlier investigations (see, e.g., Refs. [8,14,16]). The $R(t)$ anisotropy function obtained experimentally can be approximated as

$$R(t) \approx A_{22}^{\mathrm{eff}} \sum_i f_i G_{22}^i(t), \quad (4)$$

where A_{22}^{eff} corresponds to the corrected solid-angle anisotropy coefficient, and the summation over i accounts for the different observed local environments, each weighted by a population factor f_i. The experimental $R(t)$ functions were analyzed with exact numerical methods that construct the expected observable by solving the exact characteristic equation of the hyperfine interaction Hamiltonian using NNFIT software [22,27].

B. Computational details

First-principles calculations within the DFT [28,29] framework were performed using the Quantum ESPRESSO computational package [30,31]. The exchange-correlation potential was treated based on the generalized gradient approximation (GGA) to describe the electronic structure, as proposed by Perdew, Burke, and Ernzerhof (PBE) [32]. The calculations were carried out with the projected augmented wave (PAW)

method [33], which has shown to be appropriate for describing electric field gradients [34]. The wave functions and charge densities were expanded in a plane wave basis set with cutoff energies 110 Ry and 600 Ry, respectively.

High-temperature and structural phase transitions were investigated by following the change of the average atomic positions as a function of temperature, as reported in the literature. We used experimental structural data reported for the $A2_1am$ and $Acaa$ space groups from Refs. [5] and [7] while the aristotype $I4/mmm$ phase was built from the $Acaa$ reported structure by removing the X_1^- octahedral rotation and the orthorhombic lattice deformation using the ISODISTORT web-based tool [35,36]. The $A2_1am$ ground-state properties were also obtained, self-consistently, by optimizing the structure and atomic positions until a total force smaller than 0.05 eV/Å was achieved [37]. For all of these $Ca_3Ti_2O_7$ structures, we compute the EFG components at the nonequivalent Ca sites, localized in the perovskite blocks (Ca^{PV}) or in the rocksalt-like layers (Ca^{RS}). The irreducible first Brillouin zone was sampled with a $7 \times 4 \times 4$ Monkhorst-Pack (MP) k mesh [38]. In all cases, convergence tests were performed. The inclusion of a Cd ion as a probe in the $Ca_3Ti_2O_7$ system, replacing a Ca atom in the appropriate position (Cd^{RS} or Cd^{PV}), was considered by constructing a 192-atom $2 \times 2 \times 2$ supercell, based on the primitive RP crystal structure, and the Brillouin zone was sampled by a $4 \times 2 \times 2$ MP k mesh. It is worth mentioning that this supercell size already gave converged results as tested using larger 432-atom $3 \times 3 \times 2$ supercells.

To consider relaxations and distortions around the Cd impurity, the force criterium was used by analyzing the displacement of Cd and its neighbors inside a given $r = 3.9$ Å radius around the impurity, while keeping fixed the atoms outside this region.

III. RESULTS

A. Perturbed angular correlation results

The experimental perturbation function $R(t)$ and the respective FTs are shown in Fig. 3. Throughout the measured temperature range, below 1057 K, it is possible to notice a mixture of at least two EFGs, labeled as EFG_1 and EFG_2. The coexistence of these EFGs is highlighted in the FTs graphs by the two frequency triplets identified by the blue and yellow lines. These two fractions represent two well-defined EFG distributions, portraying $R(t)$ profiles with low attenuation (low δ values). Above the 1057 K temperature, it is possible to refine the experimental $R(t)$ function considering the presence of a third (EFG_3) and a fourth (EFG_4) EFG, highlighted in the FTs graphs by the green and pink lines.

The thermal dependency of the EFG strength, $|V_{zz}|_i$, and the asymmetry parameter η_i for the different observed local environments ($i = 1$–4), are represented in Fig. 4. At room temperature, the EFG_1, identified as the blue dots in Fig. 4, is characterized by a $|V_{zz}|_1 \approx 76$ V/Å^2 with $\eta_1 \approx 0.76$, while the EFG_2, identified as the yellow dots, is characterized by a $|V_{zz}|_2 \approx 68$ V/Å^2 with $\eta_2 \approx 0.42$. For temperatures below room temperature, the strength of EFG_1 and EFG_2 are identical, but with distinct asymmetry parameters. Upon increasing
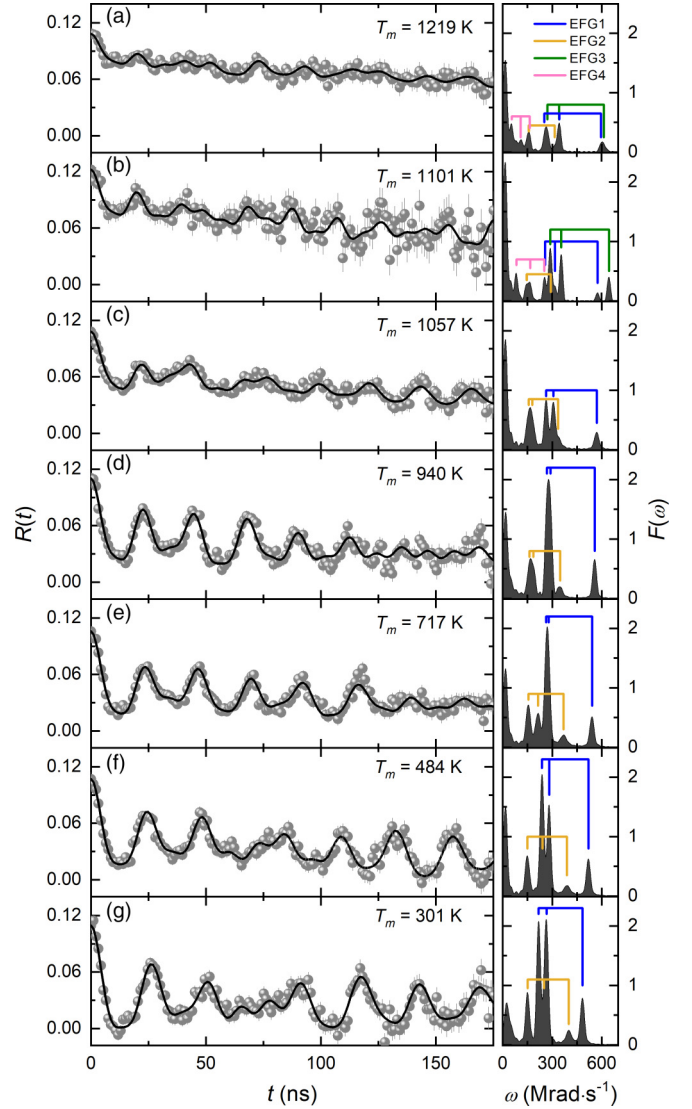

FIG. 3. Representative $R(t)$ functions with the corresponding fits, and respective Fourier transforms of the fits taken at several temperatures.

temperature, above 200 K, the thermal dependency of $|V_{zz}|_1$ and $|V_{zz}|_2$ have opposite trends: while the EFG_2 presents the standard behavior, a decrease of the $|V_{zz}|_2$ magnitude for increasing temperature, the EFG_1 presents an atypical increase of $|V_{zz}|_1$ magnitude. This latter behavior was also observed when probing the Ca^{RS} local environment in the $A2_1am$ structure of the $Ca_3Mn_2O_7$ system [14].

To assess the $|V_{zz}|_i$ trends, one can employ a linear least squares fit, allowing the derivation of a normalized slope defined as

$$\alpha_i = \frac{1}{|V_{zz}^0|_i} \frac{\Delta |V_{zz}|_i}{\Delta T}, \tag{5}$$

where $|V_{zz}^0|_i$ corresponds to the intercept obtained from the fit. Table I, presents the respective α_i values. An average positive coefficient $\alpha_1 = 2.8(2) \times 10^{-4}$ K^{-1} was obtained in the 10–1220 K temperature range for the EFG_1, which is of the
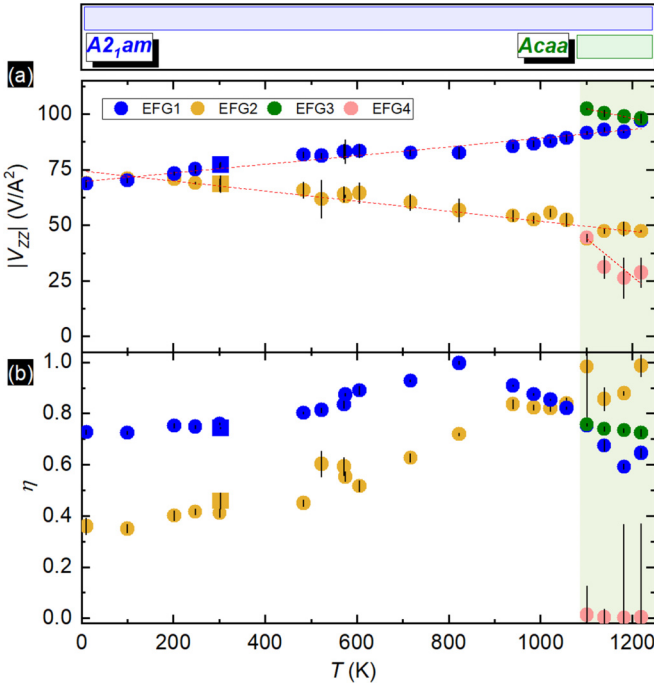
FIG. 4. Experimental results for the Ca$_3$Ti$_2$O$_7$ sample. (a) EFG strength $|V_{zz}|$ and (b) asymmetry parameter η. The dashed red line represents the linear least squares fits. The square symbols highlight the fitting parameters obtained when increasing the postimplantation annealing temperature to 1283 K.

same order of magnitude of that for the Ca$_3$Mn$_2$O$_7$ compound in the $A2_1am$ structural phase (2.3×10^{-4} K^{-1}) [14].

However, for the Ca$_3$Ti$_2$O$_7$ system, a close inspection of $|V_{zz}|_1$ trend reveals two peculiar slope changes within the 500–900 K temperature range (highlighted in Fig. 8 of Appendix B). A slope decrease of $|V_{zz}|_1$ is observed at ≈ 500 K. This behavior reflects the local structural changes that underlie the gradual Ca$_3$Ti$_2$O$_7$ ferroelectric polarization (P) decrease, reported to be significant between 500–800 K temperature range [13]. The second $|V_{zz}|_1$ trend change occurs concomitantly with the increase of the asymmetry parameter towards $\eta_1 \approx 1$ (≈ 823 K). As highlighted in Appendix B, where the derived $|V_{yy}|_1$ and $|V_{xx}|_1$ components are also shown, such $|V_{zz}|_1$ trend behavior reflect an EFG principal axes permutation, observed when the magnitude of $|V_{zz}|_1$ and $|V_{yy}|_1$ become identical. This occurs due to the convention $|V_{zz}| \geqslant |V_{yy}| \geqslant |V_{xx}|$ without necessarily indicating a change in the crystal's symmetry structure. This phenomenon was

TABLE I. Experimental $|V_{zz}|_i$ thermal trends, obtained from linear fits, carried within the 10–1220 K temperature range for EFG$_1$ and EFG$_2$, and within 1100–1220 K for EFG$_3$ and EFG$_4$.

EFG$_i$	$\Delta|V_{zz}|_i/\Delta T$ ($\times 10^{-2}$ VÅ^{-2}K^{-1})	α_i ($\times 10^{-4}$ K^{-1})
EFG$_1$	1.9 ± 0.1	2.8 ± 0.2
EFG$_2$	-2.2 ± 0.1	-3.0 ± 0.1
EFG$_3$	-4.2 ± 0.2	-2.9 ± 0.1
EFG$_4$	-17 ± 6	-7.4 ± 0.4

already observed in EFG vs P theoretical DFT-based studies, focused on ferroelectric polarization switching paths via changing the amplitude of the TiO$_6$ rotation or tilting modes of several RP structures [15].

On the other hand, for EFG$_2$, a continuous $|V_{zz}|_2$ decrease is observed, characterized with an average negative coefficient $\alpha_2 = -3.0(1) \times 10^{-4}$ K^{-1}, which is similar to the order of magnitude of the values reported when probing the A site in perovskite oxide structures [39].

In the 11–1219 K temperature range, the ^{111m}Cd probe distributions average ratio ($f_{\text{EFG}_1} : f_{\text{EFG}_2}$) is $\sim 2 : 1$. This agrees with the inequivalent Ca^{RS} to Ca^{PV} ratio of available sites in the Ca$_3$Ti$_2$O$_7$ unit cells, as previously depicted in Fig. 1. This fact suggests that the Cd probes are well distributed between both positions after the post-implantation annealing procedure.

The EFG$_3$, observed for temperatures higher than 1100 K, represented as the green circles in Fig. 4, is characterized by a $|V_{zz}|_3 \approx 102$ V/A^2 with $\eta_3 \approx 0.76$. Furthermore, above 1100 K the strength of the EFG$_3$ decreases with increasing temperature, which is similar to the behavior observed when probing the Ca^{RS} local environment in the $Acaa$ Ca$_3$Mn$_2$O$_7$ structure [14]. Within the 1100–1220 K temperature range, an average negative coefficient of $\alpha_3 = -2.9(1) \times 10^{-4}$ K^{-1} was obtained. The high value for the asymmetry parameter of the EFG$_3$ is not in agreement with the interpretation of a transition to the aristotype $I4/mmm$ tetragonal phase, but otherwise with a transition to the locally distorted $Acaa$ orthorhombic structure, as the DFT calculations presented in the next section corroborate. The presence of an extra EFG$_4$ could also be observed in this high-temperature range. At 1101 K the EFG$_4$ is characterized by a magnitude of $|V_{zz}|_4 \approx 44$ V/A^2 with $\eta_4 \approx 0$. For higher temperatures, the asymmetry parameter remains low. However, the estimation of the EFG parameters for this distribution was harder to access from the fits, due to the respective lower occupation and the growing contribution of possible local decomposition of the Ca$_3$Ti$_2$O$_7$ system at high temperatures, as detailed in Appendix C. Still, the obtained ($f_{\text{EFG}_3} : f_{\text{EFG}_4}$) probe weight distribution average ratio 1.8:1, across the 1101–1219 K temperature range, remains similar to the 2:1 ratio of available Ca^{RS} : Ca^{PV} sites in the RP structures.

The following DFT calculations focus on the nature of the structural phase transition of the Ca$_3$Ti$_2$O$_7$ compound, taking into account the effects of Cd-ion substitution at various Ca sites in the Ca$_3$Ti$_2$O$_7$ system under the distinct structural symmetries.

B. DFT calculations

1. ^{111m}Cd as a probe within the DFT determined $A2_1am$ ground state structure

Table II shows the theoretical EFG results for the substitutional Cd at Ca atomic positions, Cd^{PV} and Cd^{RS}, for the Ca$_3$Ti$_2$O$_7$ 192-atom supercell on the polar $A2_1am$ ground-state phase. For comparison, it is also shown the respective EFG values at the Ca^{PV} and Ca^{RS} sites in the undoped material. One notices that the Ca substitution and the relaxation/distortion introduced by Cd, produce a large variation of the EFG parameters: an increase factor ~ 2.8 is

TABLE II. EFG principal component $|V_{zz}|$, in units of V/Å^2, and asymmetry parameter η, dimensionless for the theoretically obtained ground state $A2_1am$ phase of the Ca$_3$Ti$_2$O$_7$ 192-atom supercell. The values of $|V_{zz}|$ and η at the Ca^{PV} (perovskite) and Ca^{RS} (rocksalt) sites are shown, amongst the respective values at the Cd site replacing the Ca atoms at both nonequivalent positions, Cd^{PV} and Cd^{RS}.

Ground state $A2_1am$ structure	$|V_{zz}|$	η
Ca$_3$Ti$_2$O$_7$: Cd^{PV}	61	0.47
Ca$_3$Ti$_2$O$_7$: Ca^{PV}	22	0.59
Ca$_3$Ti$_2$O$_7$: Cd^{RS}	44	0.63
Ca$_3$Ti$_2$O$_7$: Ca^{RS}	24	0.89

observed in the PV site, whereas in the RS site, the factor is ~ 1.8. The latter ratio is in good agreement with the expected ~ 1.9 EFG enhancement due to the polarization of the Cd probe's internal orbitals, arising purely from the ionic lattice in the point charge model [25].

The results displayed in Table II indicate that structural relaxation effects are more important when substitutional Cd occupies the Ca PV site (rather than the RS), what can be understood by the fact that the PV sites have more nearest-neighbors, especially oxygen ligand atoms.

We performed an energetic analysis of the substitutional Cd in the $A2_1am$ polar phase of the Ca$_3$Ti$_2$O$_7$ system ground state, using the 192-atom supercell. The total energy difference between the supercells containing either the Cd^{RS} or Cd^{PV} substitutional impurity is $\Delta E \sim 0.3$ eV (per supercell), in favor of the Ca^{RS} site. That ΔE value is similar to the one found for the Ca$_3$Mn$_2$O$_7$ compound [14]. However, a fundamental feature differentiates Ca$_3$Mn$_2$O$_7$ and Ca$_3$Ti$_2$O$_7$: While replacement of Ca by Cd in the RS site is favored in the Mn case [14], in the Ti-based perovskite, a coexistence of two fractions can be observed in the PAC measurements. These behaviors may be related to distinct energy barriers between the two energy minima of Cd-substitutional sites in the Mn- and Ti-based compounds, which might change the migration profiles of the Cd probes postimplantation.

2. ^{111m}Cd as a probe within the experimental determined low temperature $A2_1am$ structure

Supercell calculations were performed also using the experimental reported $A2_1am$ phase structures [5,7], at the low 125 K temperature. Table III shows the DFT theoretical EFG results for the substitutional Cd^{PV} and Cd^{RS}, and for comparison, the values obtained at the Ca^{PV} and Ca^{RS} for the pristine (undoped) 125-K structure are also shown. Noticeably, the new value of $|V_{zz}|$ for the Ca^{RS} site is higher (32 V/Å^2) than the obtained using the determined ground-state structure (24 V/Å^2). In comparison, the new value obtained for the Ca^{PV}-site (21 V/Å^2) remains similar to the one obtained in the previously studied structure (22 V/Å^2). After performing the Ca by Cd substitution for both sites, independently, the strength of the EFG approximately doubles at each case: 21 to 41 V/Å^2, at the PV site, and 32 to 60 V/Å^2 at the RS site. After performing structural relaxation of Cd probes' nearest neighbors, for both sites up to a distance of 3.9 Å, the strength of the Cd EFG remains similar at the RS site,

TABLE III. EFG principal component $|V_{zz}|$, in units of V/Å^2, and asymmetry parameter η, dimensionless, for the $A2_1am$ phase of the Ca$_3$Ti$_2$O$_7$ 192-atom supercell, obtained for the structural parameters at 125 K reported in Ref. [5]. The values at the Ca^{PV}, Ca^{RS}, Cd^{PV}, and Cd^{RS} nuclei are shown. The EFG parameters for the Cd nuclei sites are displayed for before ($|V_{zz}|$, η) and after ($|V_{zz}|_{rlx}$, η_{rlx}) atomic positions relaxations.

125 K $A2_1am$ structure	$|V_{zz}|$	η	$|V_{zz}|_{rlx}$	η_{rlx}
Ca$_3$Ti$_2$O$_7$: Cd^{PV}	41	0.99	63	0.55
Ca$_3$Ti$_2$O$_7$: Ca^{PV}	21	0.96		
Ca$_3$Ti$_2$O$_7$: Cd^{RS}	60	0.91	64	0.76
Ca$_3$Ti$_2$O$_7$: Ca^{RS}	32	0.89		

i.e., $|V_{zz}|_{rlx} = 64$ V/Å^2 versus $|V_{zz}| = 60$ V/Å^2, while it increases at Cd^{PV} from $|V_{zz}| = 41$ V/Å^2 to $|V_{zz}|_{rlx} = 63$ V/Å^2. These EFGs obtained at Cd^{PV} and Cd^{RS} sites, after relaxation, are in very good agreement with the experimental values, as shown in Fig. 4, where two distinct local environments having identical EFG strengths but distinct asymmetry parameters are observed. The $|V_{zz}|$ DFT trend observed for Cd^{RS} and Cd^{PV} sites using structural data reported for the $A2_1am$ phase between temperatures of 125 and 500 K, considering the relaxation effects, presents a consistent behavior with the values obtained for the experimental structure at 125 K (Table III), as it will be discussed in the next subsection. Nevertheless, small magnitude discrepancies with experimental results could be expected due to the EFG sensitivity to temperature.

3. EFG parameters for the temperature evolution of the $A2_1am$, $Acaa$, $I4/mmm$ structures for the pristine and Cd-doped compounds

Further DFT studies regarding the EFG parameters for the polar $A2_1am$ phase thermal evolution, as well as for the high-temperature $Acaa$ and $I4/mmm$ structures, were performed. The latter simulations were conducted to clarify the nature of the third and fourth local environments experimentally observed for temperatures higher than 1100 K, as depicted in Fig. 4. Figure 5 presents the DFT calculated EFG parameters at the Ca^{PV} and Ca^{RS} sites in the Ca$_3$Ti$_2$O$_7$ structural phases. We calculated the EFGs in the polar $A2_1am$ phase using reported distinct structural lattice and atomic positions obtained for temperatures between 125 K and 1050 K. From the linear fitting of the data for the $|V_{zz}|$ trend, the normalized slope values [Eq. (5)] were extracted and are shown in Table IV. A positive α coefficient $\sim 2.5 \times 10^{-4}$ K^{-1} was obtained for both Ca^{RS} and Ca^{PV} sites, being similar to the experimental value found for the Cd probe EFG$_1$ distribution (see Table I), but disagreeing with the negative trend experimentally observed in the EFG$_2$ case.

To address the latter contribution, we have performed calculations, in the supercell scheme, by using as input the 1050 K high-temperature $A2_1am$ phase atomic positions reported in Ref. [7], to investigate the structural relaxation effects when either probing the RS or PV sites with a Cd isotope ion substituting a Ca atom site. After performing structural relaxations, the $|V_{zz}|$ magnitude at the Cd^{PV} site decreases slightly from 57 to 51 V/Å^2, while at the Cd^{RS} site,
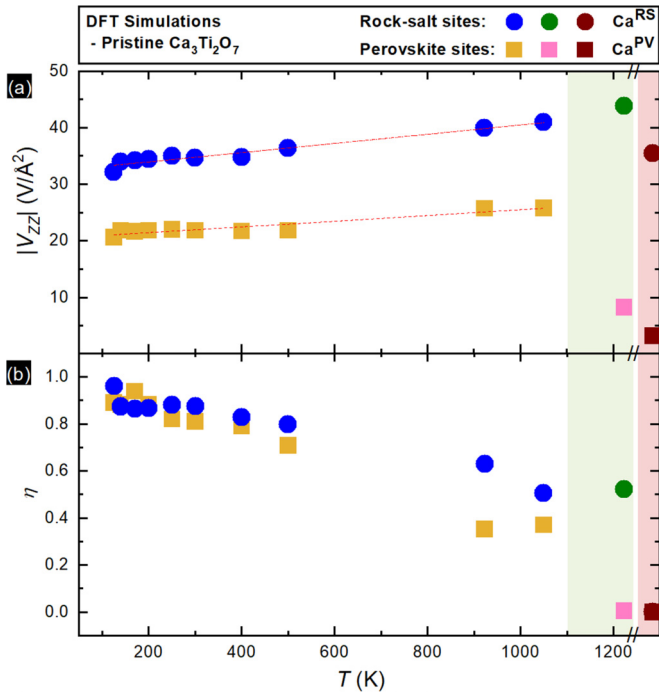
FIG. 5. EFG parameters, obtained with DFT simulations, in the Ca sites of pristine Ca$_3$Ti$_2$O$_7$ systems. (a) Principal component $|V_{zz}|$; (b) asymmetry parameter η. The results are plotted as a function of the corresponding temperature where the diffraction measurements (Refs. [5] and [7]) of the atomic positions, for $A2_1am$ and $Acaa$ phases, used as input in the DFT calculations are performed. For the aristotype $I4/mmm$ phase, the simulated structure was built by removing the lattice and octahedral distortions of the $Acaa$ reported structure through the ISODISTORT tool [35,36]. White, green, and red graphs regions correspond to $A2_1am$, $Acaa$, and $I4/mmm$ phases, respectively.

the EFG strength increases from 81 to 103 V/Å^2, as can be observed in Table V. As visually depicted in Fig. 6(a), the structural relaxation of Cd, together with its neighboring ions, induces a change in the slope of the trend, as a function of temperature, of $|V_{zz}|$ values at the $A2_1am$ PV site. The results of the supercells calculations show that the effects of structural relaxation around the probe are important for an adequate description of the systems, and that when they are taken into account the $|V_{zz}|$ values in the Cd^{PV} and Cd^{RS} sites exhibit opposite trends, as observed experimentally. Furthermore, interestingly, when comparing the results presented in Figs. 4(b) and 6(b), we can realize that the interchange of the η's values

TABLE IV. DFT results of the $|V_{zz}|$ thermal trends obtained from linear fitting at the Ca and Cd sites in the polar $A2_1am$ phase, for the pristine and doped supercell structures.

Atomic sites	$\Delta|V_{zz}|/\Delta T$ ($\times 10^{-2}$ VÅ^{-2}K^{-1})	α ($\times 10^{-4}$ K^{-1})
Ca^{RS}	0.81 ± 0.06	2.5 ± 0.2
Ca^{PV}	0.51 ± 0.06	2.5 ± 0.4
Cd^{RS}	4.2	7.2
Cd^{PV}	-1.3	-2.0

TABLE V. EFG principal component $|V_{zz}|$, in units of V/Å^2, and asymmetry parameter η, dimensionless, for the $A2_1am$ phase of the Ca$_3$Ti$_2$O$_7$ 192-atom supercell, obtained for the structural parameters at 1050 K reported in Ref. [7]. The values at the Ca^{PV}, Ca^{RS}, Cd^{PV}, and Cd^{RS} nuclei are shown. The parameters for the Cd nuclei sites are shown before and after atomic positions relaxation (rlx).

1050 K $A2_1am$ structure	$|V_{zz}|$	η	$|V_{zz}|_{\mathrm{rlx}}$	η_{rlx}
Ca$_3$Ti$_2$O$_7$: Cd^{PV}	57	0.27	51	0.65
Ca$_3$Ti$_2$O$_7$: Ca^{PV}	26	0.37		
Ca$_3$Ti$_2$O$_7$: Cd^{RS}	81	0.66	103	0.62
Ca$_3$Ti$_2$O$_7$: Ca^{RS}	41	0.60		

between the EFG$_1$ and EFG$_2$ fractions is captured by the Cd^{PV} and Cd^{RS} centers when relaxation is considered.

Regarding the pristine Ca$_3$Ti$_2$O$_7$ high-temperature $Acaa$ and $I4/mmm$ structural phases, the experimental η asymmetry parameter is expected to be zero for the PV sites of both phases and for the RS site of the undistorted high-symmetry $I4/mmm$ phase, as shown in Fig. 5. In turn, a higher asymmetry value is expected only for the RS position of the $Acaa$ phase. To confirm such expectations, EFG parameters were also theoretically obtained for the Cd nuclei
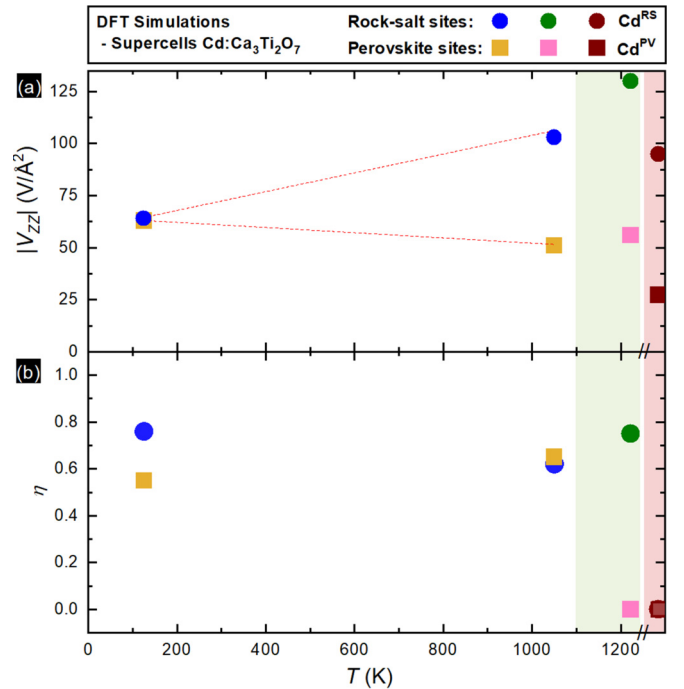

FIG. 6. EFG parameters, obtained with DFT simulations, in the Cd sites of the Cd-doped Ca$_3$Ti$_2$O$_7$ compounds. (a) Principal component $|V_{zz}|$; (b) asymmetry parameter η. The results are plotted as a function of the corresponding temperature where the diffraction measurements (Refs. [5] and [7]) of the atomic positions, for $A2_1am$ and $Acaa$ phases, used as input in the DFT calculations are performed. For the aristotype $I4/mmm$ phase, the simulated structure was built by removing the lattice and octahedral distortions of the $Acaa$ reported structure through the ISODISTORT tool [35,36]. White, green, and red graphs regions correspond to $A2_1am$, $Acaa$, and $I4/mmm$ phases, respectively.

TABLE VI. EFG principal component $|V_{zz}|$, in units of V/Å^2, and asymmetry parameter η, dimensionless, for the *Acaa* phase of the Ca$_3$Ti$_2$O$_7$ 192-atom supercell, obtained for the structural parameters at 1223 K, reported in Ref. [7], and for a hypothetical $I4/mmm$ phase. The values at the Ca^{PV} and Ca^{RS} sites are shown, amongst the respective values at the Cd site replacing the Ca atoms at both nonequivalent positions Cd^{PV} and Cd^{RS}. The EFG parameters for the Cd nuclei sites are shown before and after atomic positions relaxation (rlx).

1223 K *Acaa* structure	$|V_{zz}|$	η	$|V_{zz}|_{\mathrm{rlx}}$	η_{rlx}
Ca$_3$Ti$_2$O$_7$: Cd^{PV}	17	0	56	0
Ca$_3$Ti$_2$O$_7$: Ca^{PV}	8	0		
Ca$_3$Ti$_2$O$_7$: Cd^{RS}	87	0.60	130	0.75
Ca$_3$Ti$_2$O$_7$: Ca^{RS}	43	0.55		
$I4/mmm$ structure	$|V_{zz}|$	η	$|V_{zz}|_{\mathrm{rlx}}$	η_{rlx}
Ca$_3$Ti$_2$O$_7$: Cd^{PV}	7	0	27	0
Ca$_3$Ti$_2$O$_7$: Ca^{PV}	3	0		
Ca$_3$Ti$_2$O$_7$: Cd^{RS}	74	0	95	0
Ca$_3$Ti$_2$O$_7$: Ca^{RS}	35	0		

in the Cd-doped Ca$_3$Ti$_2$O$_7$ supercell systems, considering the *Acaa* space group by using the experimental structural data, at 1223 K, reported in Ref. [7] and the extrapolated $I4/mmm$ structure. The results are shown in Table VI. Indeed, the results show that η is only nonzero when the Cd ion occupies the Ca^{RS} site of the *Acaa* structural phase, being $\eta \sim 0.6$ in the nonoptimized case and $\eta \sim 0.75$ when atomic relaxations were taken into account. These values, when compared to the ones obtained from the PAC experiments, shown in Fig. 4, corroborate that the EFG$_3$ observed at high temperatures corresponds to the probing of Cd at the Ca^{RS} site of the *Acaa* phase. This observation supports the conclusion that the high-temperature phase transition of Ca$_3$Ti$_2$O$_7$ involves a first-order structural transition from the polar $A2_1am$ phase to the *Acaa*, in agreement with Pomiro *et al.* [7], and similar to what was reported for the Ca$_3$Mn$_2$O$_7$ system [5,14]. This confirms that both $A2_1am$ and *Acaa* structural phases coexist up to 1219 K and contradicts the commonly reported avalanche structural transition (see Fig. 2) from the polar $A2_1am$ to the aristotype $I4/mmm$ phase [6,11,12].

C. Outlook: PAC applied to uncover phase transitions in related $n = 2$ Ruddlesden-Popper systems

This local probe technique could be highly effective in investigating other Ruddlesden-Popper (RP) systems, particularly in providing corroboration or refutation of results obtained through scattering-based methods. For instance, at high temperatures, a transition from *Acaa* to $I4/mmm$ has been suggested around 870 K, for the Sr$_3$Sn$_2$O$_7$ system [40]. However, according to the atomic mechanisms supporting the uniaxial negative thermal expansion (NTE), the NTE persistence in the $I4/mmm$ symmetry suggests that the critical temperature may be higher [16,40]. The measurement of EFG at the equivalent Sr^{RS} site would allow us to discern between these two crystal symmetries as studied herein.

In the closely related Ti-based RP systems, such as the Ca$_2$SrTi$_2$O$_7$ compound, the room-temperature phase is re-

ported to be no longer the polar $A2_1am$ but a slightly distorted tetragonal $P4_2mnm$ phase [6]. The subtle local structure differences between the $P4_2mnm$ and $I4/mmm$ phases suggest that small asymmetry parameters are expected at both RS and PV A sites. Room-temperature PAC measurements should provide clear significant differences to those obtained in the Ca$_3$Ti$_2$O$_7$ system and low-temperature measurements on the Ca$_2$SrTi$_2$O$_7$ can be pursued to confirm whether the $P4_2mnm$ phase remains stable to low temperatures or undergoes a series of structural transitions to reach the polar $A2_1am$ phase, as in the Ca$_{2.15}$Sr$_{0.85}$Ti$_2$O$_7$ case. The second-order transitions between the $I4/mmmm$, $P4_2mnm$, and $Pnnm$ phases reported in Ref. [7] could only provide subtle changes in the slope of $|V_{zz}|$'s thermal behavior, but the transition between the *Amam* and $A2_1am$ phases should lead to significant changes in the asymmetry parameter, as previous DFT studies on the similar Ca$_3$Mn$_2$O$_7$ system suggest [15]. For instance, in the absence of octahedra X$_2^+$ rotation and coupled Ca-atomic displacements, the asymmetry parameter at the RS site for *Amam* structure is predicted to be ≈ 0 [15], while for $A2_1am$ structure it is ≈ 0.8, as measured here. Still as shown in this paper, the calculation of axial asymmetry and expected $|V_{zz}|$ magnitude for distinct crystal symmetry phases should always take into account the probe-induced structural relaxation effects, as performed in the supercell calculations scheme.

IV. CONCLUSIONS

PAC spectroscopy, combined with *ab initio* calculations, has proven to be a valuable tool for probing the octahedral rotations of the hybrid improper ferroelectric Ca$_3$Ti$_2$O$_7$. Local probe experimental data was acquired in a broad temperature range, and *ab initio* calculations were conducted to account for Cd ions substitutionally occupying the Ca sites in the Ca$_3$Ti$_2$O$_7$ crystal lattice across distinct structural symmetries. The results revealed that Cd probes occupy both Ca rock-salt and Ca perovskite sites in the low-temperature $A2_1am$ phase. The EFG temperature dependency at the rock-salt calcium sites, within the $A2_1am$ temperature stability, is also shown to be sensitive to the recently proposed Ca$_3$Ti$_2$O$_7$ ferroelectric polarization sharp decrease within the 500–800 K temperature range. Furthermore, the analyses indicate that the structural phase transition of the low-temperature polar phase $A2_1am$, as the temperature increases, occurs at a temperature above 1057 K, leading to a crystalline structure of orthorhombic symmetry, which belongs to the space group *Acaa*, contrary to what has often been reported as an avalanche structural transition to the $I4/mmm$ aristotype high-symmetry tetragonal phase. The $A2_1am$ and the *Acaa* structural phases are shown to coexist up to 1219 K.
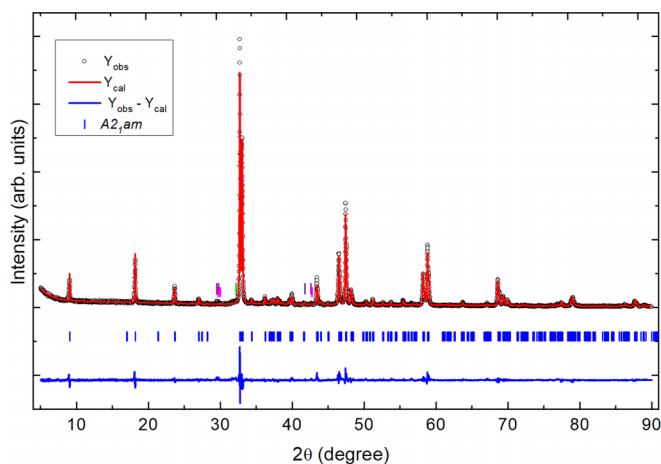
FIG. 7. Rietveld refinement to data collected by Cu-K$_\alpha$ radiation x-ray diffraction for Ca$_3$Ti$_2$O$_7$ at room temperature. The intensities of the observed pattern are plotted as black open circles. The calculated pattern is displayed as the red line and the difference between the calculated and measured diffractogram is the blue line. Blue ticks represent Bragg reflections for the Ca$_3$Ti$_2$O$_7$ $A2_1am$ spacegroup, and the purple ticks represent Bragg reflections for nonabsorbed Cu-K$_\beta$ radiation for the $A2_1am$ spacegroup as well. Pink and green ticks highlight the Bragg peaks related to a minor presence of intermediary CaTiO$_3$ and CaO compounds.

TABLE VII. Crystallographic lattice parameters (in Å) and atomic positions obtained from Rietveld Refinement for the Ca$_3$Ti$_2$O$_7$ $A2_1am$ structure.

Lattice Parameters	a	b	c
	5.4175(1)	5.4131(1)	19.5125(1)
Atom	x	y	z
Ca1	0.00000	0.25000	0.00000
Ca2	0.0494(9)	0.2389(6)	0.18899(8)
Ti	0.0282(17)	0.2490(10)	0.39831(10)
O1	0.035(5)	0.675(3)	0.00000
O2	0.016(3)	0.300(2)	0.2977(3)
O3	0.819(3)	−0.031(2)	0.3879(3)
O3	0.238(3)	0.544(2)	0.4094(3)

APPENDIX A: CRYSTALLOGRAPHIC DATA OF Ca$_3$Ti$_2$O$_7$ STUDIED SAMPLE AT ROOM TEMPERATURE

The synthesized sample's crystallographic structure and lattice parameters have been checked and refined employing XRD at room temperature, as shown in Fig. 7, where Rietveld analysis was performed using the refinement Fullprof software package [19]. An $A2_1am$ structural phase was considered to fit the diffraction pattern, achieving a $\chi^2 = 2.08$ fit goodness. The crystallographic parameters and atomic positions obtained from the refinement are shown in Table VII.

APPENDIX B: EFG$_1$: $|V_{zz}|_1$, $|V_{yy}|_1$, $|V_{xx}|_1$ THERMAL TRENDS (PROBING $A2_1am$ PHASE AT THE CALCIUM ROCK-SALT SITE)

EFG$_1$ experimental thermal trends for $|V_{zz}|_1$, $|V_{yy}|_1$, and $|V_{xx}|_1$ in the 10–1220 K temperature range for probing the $A2_1am$ phase of the Ca$_3$Ti$_2$O$_7$ compound are shown in Fig. 8.

APPENDIX C: LOW STRENGTH AND BROAD EFG DISTRIBUTION INDUCED BY HIGH-TEMPERATURE ANNEALING/MEASUREMENT CONDITIONS IN THE Ca$_3$Ti$_2$O$_7$ COMPOUND

An important observed phenomenon in fitting the experimental results is the need to add an extra phase associated with an extra EFG distribution of low strength and relative high line broadening. In the perturbation functions represented in Fig. 9, this EFG distribution effect is highlighted by the damped and gradual time-changing individual contribution to $R(t)$ represented by the brown lines (labeled as EFG^{extra}). The probe weight of this distribution (f_i) depends on the postimplantation annealing (T$_{annealing}$) or the PAC measurement temperature (T$_m$). Particularly, this annealing temperature effect is highlighted in Fig. 9, where the experimental $R(t)$ functions were measured for identical temperatures ($\approx$300 K), but the postimplantation annealing was performed at 1283 K and 1115 K, respectively. The range of these annealing temperatures crosses the 1150 K value, for which decomposition of the Ca$_3$Ti$_2$O$_7$ structure was reported to be noticeable in high-temperature XRD measurements [5]. The respective probe occupation of this low-strength EFG
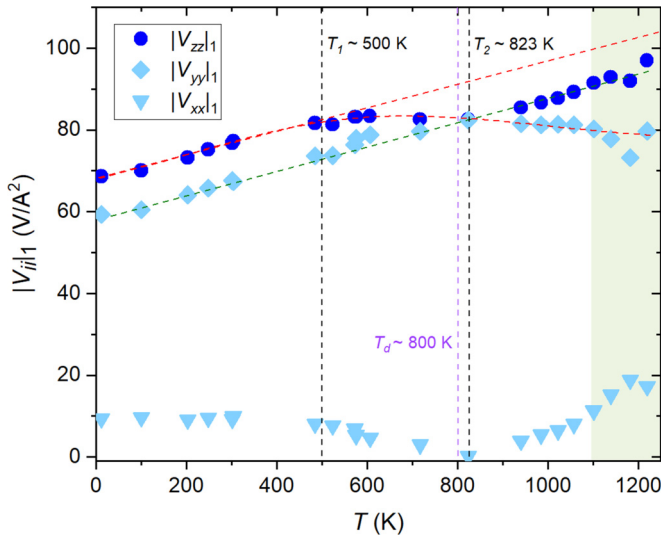
FIG. 8. Experimental thermal trends within the 10–1220 K temperature range for $|V_{zz}|_1$ and derived $|V_{yy}|_1$, $|V_{xx}|_1$. T_1 and T_2 delimit the temperature window where slope changes in $|V_{zz}|_1(T)$ are observed. Dashed red and green lines atop the experimental data serve as visual guides to highlight these trend changes in $|V_{zz}|_1$ and $|V_{yy}|_1$. $T_1 \approx 500$ K highlights gradual local structure changes following the reported decrease in $Ca_3Ti_2O_7$ ferroelectric polarization, where it was reported that at $T_d \approx 800$ K the polarization behavior of $Ca_3Ti_2O_7$ eventually transitions from a three-dimensional universality class to a two-dimensional Ising model [13]. While $T_2 \approx 823$ K marks an EFG principal axes permutation when the magnitude of $|V_{zz}|_1$ and $|V_{yy}|_1$ become identical. This occurs due to the convention $|V_{zz}| \geqslant |V_{yy}| \geqslant |V_{xx}|$ without necessarily indicating a change in the crystal's symmetry structure.

FIG. 9. Comparing the effects of increasing the post-implantation annealing temperature ($T_{annealing}$) from 1115 K to 1283 K, by measuring afterward the respective $R(t)$ function near room-temperature conditions. (a) $T_m = 301$ K and (b) $T_m = 303$ K. The corresponding fits are shown as the black lines and the individual contributions of the EFG_1, EFG_2, and EFG^{extra} distributions to the fits are also shown by the blue, yellow, and brown lines. The respective Fourier transforms of the fits are also displayed.

distribution increased from 23% up to 58%. Considering the case of static line broadening, such EFG distribution represents the probe fraction subjected to a large number of defects, where the average effect leads to a damped $R(t)$ partial function. The nature of this field distribution may result from
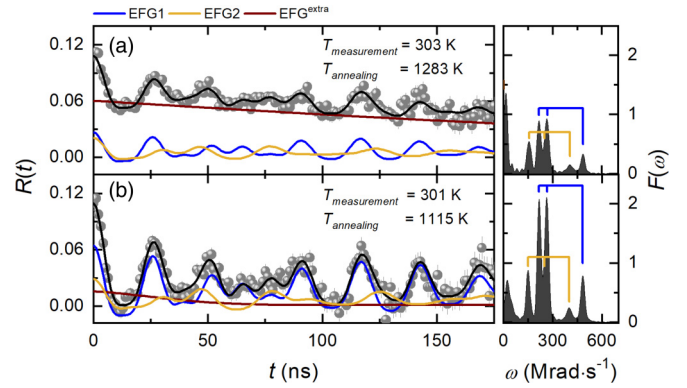
combined effects of the defects induced in the ^{111m}Cd beam implantation process and of a local $Ca_3Ti_2O_7$ partial decomposition under high-temperature conditions. The thermal stability of the $Ca_3Ti_2O_7$ and $Ca_3Mn_2O_7$ systems, including the stability limit of the NLP structures to the degree of Ca by Cd substitution, has been studied previously. In this previous DFT-based study [41], it was observed that the Ti-based system is more prone to decomposition than the Mn-based one, into the respective CaO and parent perovskite phases of $CaTiO_3$ and $CaMnO_3$. Particularly, the CaO phase as described in the cubic $Fm\bar{3}m$ space group, is expected to have null $|V_{zz}|$ at the calcium nuclear sites and could be one of the sources of this low-strength EFG distribution. Another source for this EFG distribution may be related to the probing of noncrystalline environments such as grain boundaries. However, the exact nature of this damped distribution is beyond the scope of this paper.

[1] N. A. Benedek and C. J. Fennie, Hybrid improper ferroelectricity: A mechanism for controllable polarization-magnetization coupling, Phys. Rev. Lett. **106**, 107204 (2011).

[2] Y. S. Oh, X. Luo, F.-T. Huang, Y. Wang, and S.-W. Cheong, Experimental demonstration of hybrid improper ferroelectricity and the presence of abundant charged walls in $(Ca, Sr)_3Ti_2O_7$ crystals, Nat. Mater. **14**, 407 (2015).

[3] A. B. Harris, Symmetry analysis for the Ruddlesden-Popper systems $Ca_3Mn_2O_7$ and $Ca_3Ti_2O_7$, Phys. Rev. B **84**, 064116 (2011).

[4] F. Ye, J. Wang, J. Sheng, C. Hoffmann, T. Gu, H. J. Xiang, W. Tian, J. J. Molaison, A. M. dos Santos, M. Matsuda, B. C. Chakoumakos, J. A. Fernandez-Baca, X. Tong, B. Gao, J. W. Kim, and S.-W. Cheong, Soft antiphase tilt of oxygen octahedra in the hybrid improper multiferroic $Ca_3Mn_{1.9}Ti_{0.1}O_7$, Phys. Rev. B **97**, 041112(R) (2018).

[5] M. S. Senn, A. Bombardi, C. A. Murray, C. Vecchini, A. Scherillo, X. Luo, and S. W. Cheong, Negative thermal expansion in hybrid improper ferroelectric Ruddlesden-Popper perovskites by symmetry trapping, Phys. Rev. Lett. **114**, 035701 (2015).

[6] M. Kratochvilova, F. T. Huang, M. T. F. Diaz, M. Klicpera, S. J. Day, S. P. Thompson, Y. S. Oh, B. Gao, S. W. Cheong, and J. G. Park, Mapping the structural transitions controlled by the trilinear coupling in $Ca_{3-x}Sr_xTi_2O_7$, J. Appl. Phys. **125**, 244102 (2019).

[7] F. Pomiro, C. Ablitt, N. C. Bristowe, A. A. Mostofi, C. Won, S. W. Cheong, and M. S. Senn, From first- to second-order phase transitions in hybrid improper ferroelectrics through entropy stabilization, Phys. Rev. B **102**, 014101 (2020).

[8] E. L. da Silva, A. M. Gerami, P. N. Lekshmi, M. L. Marcondes, L. V. C. Assali, H. M. Petrilli, J. G. Correia, A. M. L. Lopes, and

J. P. Araújo, Group theory analysis to study phase transitions of quasi-2D Sr₃Hf₂O₇, Nanomaterials **11**, 897 (2021).

[9] M. C. B. Barbosa, E. L. da Silva, P. N. Lekshmi, M. L. Marcondes, L. V. C. Assali, H. M. Petrilli, A. M. L. Lopes, and J. P. Araújo, Pressure-induced phase transformations of quasi-2D Sr₃Hf₂O₇, J. Phys. Chem. C **127**, 15435 (2023).

[10] K. Momma and F. Izumi, *VESTA 3* for three-dimensional visualization of crystal, volumetric and morphology data, J. Appl. Crystallogr. **44**, 1272 (2011).

[11] X. Q. Liu, J. W. Wu, X. X. Shi, H. J. Zhao, H. Y. Zhou, R. H. Qiu, W. Q. Zhang, and X. M. Chen, Hybrid improper ferroelectricity in Ruddlesden-Popper Ca₃(Ti, Mn)₂O₇ ceramics, Appl. Phys. Lett. **106**, 202903 (2015).

[12] B. Gao, F. T. Huang, Y. Wang, J. W. Kim, L. Wang, S. J. Lim, and S. W. Cheong, Interrelation between domain structures and polarization switching in hybrid improper ferroelectric Ca₃(Mn, Ti)₂O₇, Appl. Phys. Lett. **110**, 222906 (2017).

[13] J. Kong, A. Manjón-Sanz, J. Liu, F. Marlton, T. W. Lo, D. Lei, M. R. V. Jørgensen, and A. Pramanick, Scaling behavior of order parameters for the hybrid improper ferroelectric (Ca, Sr)₃Ti₂O₇, Phys. Rev. B **107**, 224103 (2023).

[14] P. Rocha-Rodrigues, S. S. M. Santos, I. P. Miranda, G. N. P. Oliveira, J. G. Correia, L. V. C. Assali, H. M. Petrilli, J. P. Araújo, and A. M. L. Lopes, Ca₃Mn₂O₇ structural path unraveled by atomic-scale properties: A combined experimental and *ab initio* study, Phys. Rev. B **101**, 064103 (2020).

[15] S. S. M. Santos, M. L. Marcondes, I. P. Miranda, P. Rocha-Rodrigues, L. V. C. Assali, A. M. L. Lopes, H. M. Petrilli, and J. P. Araujo, Spontaneous electric polarization and electric field gradient in hybrid improper ferroelectrics: insights and correlations, J. Mater. Chem. C **9**, 7005 (2021).

[16] P. Rocha-Rodrigues, S. S. M. Santos, G. N. P. Oliveira, T. Leal, I. P. Miranda, A. M. dos Santos, J. G. Correia, L. V. C. Assali, H. M. Petrilli, J. P. Araújo, and A. M. L. Lopes, Ca₂MnO₄ structural path: Following the negative thermal expansion at the local scale, Phys. Rev. B **102**, 104115 (2020).

[17] G. N. P. Oliveira, R. C. Teixeira, R. P. Moreira, J. G. Correia, J. P. Araújo, and A. M. L. Lopes, Local inhomogeneous state in multiferroic SmCrO₃, Sci. Rep. **10**, 4686 (2020).

[18] M. B. Barbosa, J. G. Correia, K. Lorenz, R. Vianden, and J. P. Araújo, Studying electronic properties in GaN without electrical contacts using γ-γ vs e-γ perturbed angular correlations, Sci. Rep. **9**, 15734 (2019).

[19] J. Rodríguez-Carvajal, Recent advances in magnetic structure determination by neutron powder diffraction, Phys. B: Condens. Matter **192**, 55 (1993).

[20] J. Schell, P. Schaaf, and D. C. Lupascu, Perturbed angular correlations at ISOLDE: A 40 years young technique, AIP Adv. **7**, 105017 (2017).

[21] A. M. L. Lopes, J. P. Araújo, J. J. Ramasco, E. Rita, V. S. Amaral, R. Suryanarayanan, and J. G. Correia, Percolative transition on ferromagnetic insulator manganites: Uncorrelated to correlated polaron clusters, Phys. Rev. B **73**, 100408(R) (2006).

[22] J. G. Correia, H. Haas, V. S. Amaral, A. M. L. Lopes, J. P. Araújo, S. L. Floch, P. Bordet, E. Rita, J. C. Soares, and W. Tröger, Atomic ordering of the fluorine dopant in

the HgBa₂CuO₄₊δ superconductor, Phys. Rev. B **72**, 144523 (2005).

[23] M. A. Nagl, M. B. Barbosa, U. Vetter, J. G. Correia, and H. C. Hofsäss, A new tool for the search of nuclides with properties suitable for nuclear solid state physics based on the evaluated nuclear structure data files, Nucl. Instrum. Methods Phys. Res., Sect. A **726**, 17 (2013).

[24] T. Butz, Analytic perturbation functions for static interactions in perturbed angular correlations of gamma-rays, Hyperfine Interact. **52**, 189 (1989).

[25] G. Schatz and A. Weidinger, *Nuclear Condensed Matter Physics: Nuclear Methods and Applications* (Wiley, New York, 1996).

[26] L. A. Mendoza-Zelis, A. G. Bibiloni, M. C. Caracoche, A. R. Lopez-Garcia, J. A. Martinez, R. C. Mercader, and A. F. Pasquevich, Temperature dependence of the electric field gradient at Ta nuclei in hafnium pyrovanadate, Hyperfine Interact. **3**, 315 (1977).

[27] N. P. Barradas, NNFit the PAC MANual (Lisbon, Portugal, 1992).

[28] P. Hohenberg and W. Kohn, Inhomogeneous electron gas, Phys. Rev. **136**, B864 (1964).

[29] W. Kohn and L. J. Sham, Self-consistent equations including exchange and correlation effects, Phys. Rev. **140**, A1133 (1965).

[30] P. Giannozzi, O. Andreussi, T. Brumme, O. Bunau, M. B. Nardelli, M. Calandra, R. Car, C. Cavazzoni, D. Ceresoli, M. Cococcioni *et al.*, Advanced capabilities for materials modelling with Quantum ESPRESSO, J. Phys.: Condens. Matter **29**, 465901 (2017).

[31] P. Giannozzi, S. Baroni, N. Bonini, M. Calandra, R. Car, C. Cavazzoni, D. Ceresoli, G. L. Chiarotti, M. Cococcioni, I. Dabo *et al.*, QUANTUM ESPRESSO: a modular and open-source software project for quantum simulations of materials, J. Phys.: Condens. Matter **21**, 395502 (2009).

[32] R. Elmér, M. Berg, L. Carlen, B. Jakobsson, B. Noren, A. Oskarsson, G. Ericsson, J. Julien, T. F. Thorsteinsen, M. Guttormsen, G. Lovhoiden, V. Bellini, E. Grosse, C. Muntz, P. Senger, and L. Westerberg, Generalized gradient approximation made simple, Phys. Rev. Lett. **78**, 1396(E) (1997).

[33] P. E. Blöchl, Projector augmented-wave method, Phys. Rev. B **50**, 17953 (1994).

[34] H. M. Petrilli, P. E. Blöchl, P. Blaha, and K. Schwarz, Electric-field-gradient calculations using the projector augmented wave method, Phys. Rev. B **57**, 14690 (1998).

[35] B. J. Campbell, H. T. Stokes, D. E. Tanner, and D. M. Hatch, *ISODISPLACE:* a web-based tool for exploring structural distortions, J. Appl. Crystallogr. **39**, 607 (2006).

[36] H. T. Stokes, D. M. Hatch, and B. J. Campbell, ISODISTORT, ISOTROPY Software Suite, https://stokes.byu.edu/iso/isotropy.php.

[37] M. L. Marcondes, S. S. M. Santos, I. P. Miranda, P. Rocha-Rodrigues, L. V. C. Assali, A. M. L. Lopes, J. P. Araujo, and H. M. Petrilli, Cadmium-based ferroelectrics with the Ruddlesden-Popper and double perovskite structures: a theoretical study, J. Mater. Chem. C **8**, 14570 (2020).

[38] H. J. Monkhorst and J. D. Pack, Special points for Brillouin-zone integrations, Phys. Rev. B **13**, 5188 (1976).

[39] A. M. L. Lopes, J. P. Araújo, V. S. Amaral, J. G. Correia, Y. Tomioka, and Y. Tokura, New phase transition in the

$Pr_{1-x}Ca_xO_3$ system: Evidence for electrical polarization in charge ordered manganites, Phys. Rev. Lett. **100**, 155702 (2008).

[40] S. Yoshida, H. Akamatsu, R. Tsuji, O. Hernandez, H. Padmanabhan, A. Sen Gupta, A. S. Gibbs, K. Mibu, S. Murai, J. M. Rondinelli, V. Gopalan, K. Tanaka, and K. Fujita, Hybrid improper ferroelectricity in $(Sr, Ca)_3Sn_2O_7$ and beyond: Universal relationship between ferroelectric transition temperature and tolerance factor in $n = 2$ Ruddlesden-Popper phases, J. Am. Chem. Soc. **140**, 15690 (2018).

[41] M. L. Marcondes, S. S. M. Santos, I. P. Miranda, P. Rocha-Rodrigues, L. V. C. Assali, A. M. L. Lopes, J. P. Araújo, and H. M. Petrilli, On the stability of calcium and cadmium based Ruddlesden-Popper and double perovskite structures, J. Mater. Chem. C **9**, 15074 (2021).